Engineering Analysis with Boundary Elements 179 (2025) 106384

Contents lists available at ScienceDirect

Engineering Analysis with Boundary Elements

journal homepage: www.elsevier.com/locate/enganabound

Nonlocal static modeling of laminated composite shells using peridynamic differential operator in a higher-order shear deformation framework

Yonca Bab [a,b,*], Mehmet Dorduncu [c], Akif Kutlu [a], Bernd Markert [b]

[a] Department of Civil Engineering, Istanbul Technical University, Istanbul, Türkiye
[b] Institute of General Mechanics, RWTH Aachen University, Aachen, Germany
[c] Department of Mechanical Engineering, Izmir Institute of Technology, Izmir, Türkiye

ARTICLE INFO

Keywords:
Peridynamic differential operator
Higher-order shear deformation theory
Laminated composite shells
Static analysis
Nonlocal interaction

ABSTRACT

This study investigates the flexural behaviour of the laminated composite shells in the framework of Higher-Order Shear Deformation Theory (HSDT) and Peridynamic Differential Operator (PDDO), namely PD-HSDT, for the first time. Laminated composite shell structures are widely used in aerospace, automotive, and marine industries due to their high strength-to-weight ratio and design flexibility. Therefore, understanding their mechanical behavior under various loading conditions is crucial for ensuring structural reliability and performance optimization. However, such structures may possess complex curvatures and highly heterogenous laminate stackings, leading to inaccurate numerical stress analyses. The HSDT successfully captures displacement and stress distributions as well as cross-sectional warping through higher-order functions exist in the kinematics. Moreover, the PDDO represents the local derivatives in their nonlocal form, making it well-suited for problems involving higher-order derivatives and discontinuities. The governing equations and boundary conditions of the HSDT are solved by using the PDDO to accurately achieve the stress and displacement fields in the laminated composite shells. The robustness of the PD-HSDT is established by considering various loading and boundary conditions. The proposed approach demonstrates high accuracy in stress and displacement predictions when validated against reference solutions available in existing literature. This indicates strong potential for extending the methodology to more complex loading scenarios and damage mechanisms in future studies.

1. Introduction

Composite structures are crucial in industries such as aviation, nuclear power, military, automotive, construction, marine, and aerospace due to their ability to integrate various materials for diverse design objectives [1]. These structures consist of layers with distinct material properties, which can lead to stress concentrations at their interfaces, resulting in crack formation and propagation. Understanding their mechanical behavior under different loading conditions during the design phase is essential. However, experimentally assessing laminated composite structures is often costly and time-consuming [2]. Consequently, numerical modeling methods provide a more efficient and cost-effective alternative for analyzing the structural behavior of composite shells under diverse loading. Thick laminated and sandwich composites, which are essential in primary load-bearing applications, can suffer damage in fiber-rich or resin-rich layers depending on the type of loading [3]. Accurate prediction of stress and strain distributions is crucial for designing reliable composite structures and enhancing their performance. Given the time-consuming and expensive nature of structural testing and analysis, advanced and precise computational tools are indispensable for evaluating the strength of composite structures.

The finite element method is commonly employed in both academia and industry for analyzing laminated composite structures [2,4]. While traditional 3D finite element models are suitable for complex geometries, laminated composites, with their layered material properties, require high-fidelity meshes for accurate representation. Consequently, using 3D meshes for these structures can be impractical, leading to challenges in computation time and result accuracy, particularly in damage and nonlinear analysis.

Equivalent Single Layer Theories (ESL) and Layer-wise Theories (LWT) are widely preferred for analyzing laminated composite beams,

* Corresponding author at: Department of Civil Engineering, Istanbul Technical University, Istanbul, Türkiye.
E-mail addresses: bab@itu.edu.tr (Y. Bab), mehmetdorduncu@iyte.edu.tr (M. Dorduncu), kutluak@itu.edu.tr (A. Kutlu), markert@iam.rwth-aachen.de (B. Markert).

https://doi.org/10.1016/j.enganabound.2025.106384
Received 13 June 2025; Received in revised form 28 June 2025; Accepted 30 June 2025
Available online 11 July 2025

plates, and shells due to their efficiency in computation and precision, and to avoid issues associated with 3D FE meshes. LWT offers higher accuracy by calculating variables for each layer, but it can become computationally intensive with many layers. ESL, by computing the displacement field for a single equivalent layer, provides significant efficiency in computation time. The subcategories of ESL theories include Classical Laminate Theory (CLT) which follows Kirchhoff hypothesis, First-order Shear Deformation Theory (FSDT), Higher-order Shear Deformation Theory (HSDT) introduced by Reddy [5], and Zigzag theories (ZZ). CLT is convenient for homogeneous thin shells because it ignores the transverse shear strains. On the other hand, FSDT determines an average rotation of the cross-section to account for shear strains along the beam thickness and produces more realistic strain and stress results for relatively thick beams than CLT. The FSDT needs a shear correction factor to address the errors inherent in the theory. This factor is influenced by the problem's geometry, layer arrangement, boundary conditions, and loading scenarios [6,4]. Consequently, the FSDT can encounter challenges, particularly in stress analysis of thick structures (where length/thickness < 10) and those with heterogeneous properties.

HSDT overcomes the displacement and stress shortcomings of CLT and FSDT and describes the kinematic relations in terms of higher-order expressions such as polynomial, exponential, or trigonometric (also other types) functions, to better reflect the cross-sectional shear deformation. ZZ theories also provide a realistic description of in-plane deformations by introducing additional section warping functions, and the number of kinematic variables in the ZZ theory is independent of the number of material layers in the structural section.

Various forms of higher-order theories for beams [7], plates [8], and shells [9] have been extensively studied by researchers. Ermis [10] investigated curved beams applying warping included mixed Finite Element Method (FEM). Recently, Bab and Kutlu [9] summarized the researchers who worked on static or dynamic analysis of laminated composite shells applying FSDT or HSDT. Zhao et al. [11] performed static and dynamic analysis of functionally graded magneto-electro-elastic porous (FG-MEEP) cylindrical shells applying FEM and FSDT. Tornabene et al. [12] investigated the thermo-magneto-mechanical behaviour of curved laminates applying the generalized differential quadrature method and HSDT. Gupta et al. [13] presented a FEM using in-house MATLAB codes to implement sinusoidal shear deformation theory with Murakami's ZZ function for laminated composites and investigated the active damping behavior of laminated multiscale hybrid fiber-reinforced composite (HFRC) smart shells. Ly et al. [14] introduced an advanced cell-based smoothed discrete shear gap method (CS-DSG3) using ZZ theory combined with a hybrid control mechanism to analyze the smart damping control of laminated functionally graded carbon nanotube reinforced composite (FG-CNTRC) shells. Gao et al. [15,16] and Zhang et al. [17] applied the Refined Zigzag Theory (RZT) proposed by Tessler et al. [18–21] for laminated composite shells. Recently, Ermis et al [22] combined RZT with machine learning to analyse laminated composites.

Parallel to these developments, the Carrera Unified Formulation (CUF) [23,24] has emerged as a robust and versatile framework that unifies ESL and LWT, enabling the systematic derivation of refined structural models for various configurations. In recent advancements, Mir et al. [25] employed a higher-order CUF-based approach to investigate the mechanical buckling behavior of stiffened cylindrical structures, while Mohammed et al. [26] applied CUF in conjunction with a cohesive zone modeling strategy to analyze delamination phenomena in functionally graded beams.

To solve CUF-based formulations or ESL theory equations, the FEM is commonly employed through weak form implementations, relying heavily on mesh discretization to approximate spatial derivatives. However, FEM may face challenges when dealing with problems involving discontinuities, sharp gradients, or evolving geometries, as its accuracy and stability are highly dependent on mesh quality. On the other hand, mesh-free methods like radial basis function [27], Peridynamics (PD) [28–32], and nonlocal operator methods (NOM) [33] improve the handling of complex geometries and sharp gradients by using nonlocal derivatives. These methods approximate derivatives through integration within each material point's interaction domain [34,35]. In meshless methods, each material point interacts within its domain, enabling derivative approximations through integration within this domain. This approach aligns with recent advances in nanomechanics and gradient elasticity, where nonlocality is essential to capture small-scale effects, as discussed in Zur and Faghidian [36].

While meshless methods have clear benefits, implementing boundary conditions, particularly essential ones, can be challenging. Madenci et al. [37–39] recently introduced the Peridynamic Differential Operator (PDDO) to overcome these issues. This operator transforms local differentiation into a unified nonlocal integral form, effectively handling jump discontinuities and singularities. The PDDO can compute any order of derivatives through integration, maintaining nonlocal interactions [40]. Such nonlocal differential frameworks resonate with the formulations explored in Barretta et al. [41], where dissipative processes are modeled beyond the local continuum assumption, and with wave propagation studies based on unified gradient theories [42]. The PDDO introduces an internal parameter to define interactions within a finite range. As this parameter approaches zero, PDDO approximates local differentiation. It facilitates solving linear and nonlinear differential equations by connecting differentiation and integration. Recently, Dorduncu [43] and Ermis et al. [44] investigated the stress analysis of beams applying PDDO. A comprehensive review of PD formulations, including the implementation and advantages of PD operators, has been presented by Dorduncu et al. [28]. Additionally, generalizations of nonlocal gradient and micromorphic theories have been proposed in Challamel et al. [45], reinforcing the role of higher-order and two-phase nonlocality in structural modeling.

Previous research on the flexural analyses of laminated composite shells using nonlocal approaches remains limited, particularly in conjunction with higher-order theories. In this study, a novel computational framework is developed by integrating the PDDO with the HSDT, referred to as the PD-HSDT formulation, to investigate the bending response of laminated composite shells. This work marks the first attempt to combine these two approaches to overcome the limitations of existing methods in capturing both higher-order kinematics and nonlocal effects.

HSDT represents a refined form of the ESL modeling approach and offers significantly improved accuracy and computational efficiency compared to LWTs. However, its applications have traditionally been confined to local formulations. To address this, the proposed PD-HSDT method incorporates nonlocal behavior within the HSDT framework by utilizing PDDO. This method is applied to composite shells with a variety of geometries which are doubly curved, spherical, and cylindrical forms, and accommodates layer-wise variation in orthotropic material properties, making it suitable for a wide range of engineering applications.

HSDT ensures improved accuracy in capturing transverse shear effects without requiring shear correction factors, while the PDDO facilitates the nonlocal integral formulation, enabling the treatment of discontinuities and complex geometries without the need for mesh connectivity or special boundary treatments. Unlike traditional meshless methods, it eliminates the requirement for symmetric kernels or ghost particles at boundaries, simplifying implementation and enhancing accuracy. The proposed PD-HSDT model provides a balance between computational efficiency and high-fidelity stress representation. Numerical implementation is performed through an in-house FORTRAN code, and the accuracy of the method is verified against established benchmark solutions, validating its effectiveness across a range of boundary and loading conditions.

The remainder of this paper is structured as follows: Section 2 outlines the peridynamic concept, while Section 3 focuses on the

peridynamic differential operator. Section 4 summarizes the implementation of higher-order shear deformation theory. Section 5 presents several numerical analyses to evaluate the robustness of the proposed formulation under various material and lamination configurations, boundary conditions, and aspect ratios. Section 6 provides a summary and conclusion. Finally, Section 7 includes discussion and future work.

2. Concept of peridynamics

The idea of PD approach assumes that the variation of a scalar field $f = f(\mathbf{x})$, (f is valid in domain D) defined at point $\mathbf{x}$, is under the influence of the current interaction of that point with other points $\mathbf{x}'$ (see Fig. 1), [46,47]. The relative position vector directed from $\mathbf{x}$ to $\mathbf{x}'$ is denoted as $\boldsymbol{\xi} = \mathbf{x}' - \mathbf{x}$. Each material point occupies a finite region—volume in 3D or area in 2D—and interacts with all other points lying within its predefined neighbourhood $\mathbf{x}'$, referred to as the interaction domain$H_{\mathbf{x}}$.

The characteristic length scale that defines the spatial extent of nonlocal interactions in the peridynamic formulation is commonly known as the horizon. This parameter, denoted by δ, determines the size of the family—i.e., the set of neighbouring material points with which a given point interacts. The horizon size quantitatively governs the degree of nonlocality: as δ decreases, the interaction domain shrinks, and the model behavior approaches local continuum mechanics. Therefore, the family size plays a fundamental role in controlling the nonlocal character of the PD approach. Additionally, the intensity of interaction between material points is modulated by a normalized scalar weight function $w(|\boldsymbol{\xi}|)$, which depends on the relative position vector ξbetween interacting points.

3. Peridynamic differential operator

The Taylor series expansion (TSE) can be generalized for a multivariable scalar field $f(\mathbf{x}') = f(\mathbf{x} + \boldsymbol{\xi})$ in $M-$ dimensional space up to Nth order, where $n_i = 0, \ldots, N$, as [37,39]:

$$f(\mathbf{x}+\xi) = \sum_{n_1=0}^{N} \sum_{n_2=0}^{N-n_1} \cdots \sum_{n_M=0}^{N-n_1-\cdots-n_{M-1}} \frac{1}{n_1!n_2!\cdots n_M!} \xi_1^{n_1} \xi_2^{n_2} \cdots \xi_M^{n_M} \frac{\partial^{n_1+n_2+\cdots+n_M} f(\mathbf{x})}{\partial x_1^{n_1} \partial x_2^{n_2} \cdots \partial x_M^{n_M}} + R(N, \mathbf{x}) \tag{1}$$

which $R(N, \mathbf{x})$ represents the remainder of the series expansion. Thus, partial derivatives of any order can be expressed by using the orthogonal function $g_N^{p_1 p_2 \cdots p_M}(\boldsymbol{\xi})$ through the nonlocal PD approach:

$$\frac{\partial^{p_1+p_2+\cdots+p_M} f(\mathbf{x})}{\partial x_1^{p_1} \partial x_2^{p_2} \cdots \partial x_M^{p_M}} = \int_{H_{\mathbf{x}}} f(\mathbf{x}+\boldsymbol{\xi}) g_N^{p_1 p_2 \cdots p_M}(\boldsymbol{\xi}) \mathrm{d}V. \tag{2}$$

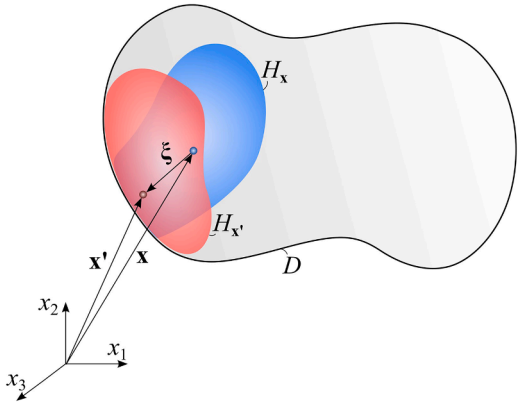

Fig. 1. Interaction of peridynamic points $\mathbf{x}$ and $\mathbf{x}'$ with arbitrary family size and shape.

Here, the contribution of the remainder is neglected. In Eq. (2) p_i stands for the order of differentiation with respect to variable x_i ($i = 1, \ldots, M$), and V is the volume of the material point $\mathbf{x}'$. The orthogonal PD functions $g_N^{p_1 p_2 \cdots p_M}(\boldsymbol{\xi})$ involves the feature of

$$\frac{1}{n_1!n_2!\cdots n_M!} \int_{H_{\mathbf{x}}} \xi_1^{n_1} \xi_2^{n_2} \cdots \xi_M^{n_M} g_N^{p_1 p_2 \cdots p_M}(\boldsymbol{\xi}) dV = \delta_{n_1 p_1} \delta_{n_2 p_2} \cdots \delta_{n_{M-1} p_{M-1}} \delta_{n_M p_M}, \tag{3}$$

and δ_{ij} is the Kronecker delta. The orthogonal PD functions can be generated as

$$g_N^{p_1 p_2 \cdots p_M}(\boldsymbol{\xi}) = \sum_{q_1=0}^{N} \sum_{q_2=0}^{N-q_1} \cdots \sum_{q_M=0}^{N-q_1-\cdots-q_{M-1}} a_{q_1 q_2 \cdots q_M}^{p_1 p_2 \cdots p_M} w_{q_1 q_2 \cdots q_M}(|\boldsymbol{\xi}|) \xi_1^{q_1} \xi_2^{q_2} \cdots \xi_M^{q_M}, \tag{4}$$

where the weight functions $w_{q_1 q_2 \cdots q_M}(|\boldsymbol{\xi}|)$ are associated with each term $\xi_1^{q_1} \xi_2^{q_2} \cdots \xi_M^{q_M}$ in the polynomial expansion. The weight function indicating the degree of interaction for each term in the Taylor series expansion may be the same or different, being related to the nature of the nonlocality.

The unknown parameters $a_{q_1 q_2 \cdots q_M}^{p_1 p_2 \cdots p_M}$ shown in Eq. (4), can be obtained from the solution of the set of linear algebraic equations established as follows:

$$\sum_{q_1=0}^{N} \sum_{q_2=0}^{N-q_1} \cdots \sum_{q_M=0}^{N-q_1-\cdots-q_{M-1}} A_{(n_1 n_2 \cdots n_M)(q_1 q_2 \cdots q_M)} a_{q_1 q_2 \cdots q_M}^{p_1 p_2 \cdots p_M} = b_{n_1 n_2 \cdots n_M}^{p_1 p_2 \cdots p_M}, \tag{5}$$

where $q_i = 0, \ldots, N$. The terms of the coefficient (shape) matrix are calculated as follows.

$$A_{(n_1 n_2 \cdots n_M)(q_1 q_2 \cdots q_M)} = \int_{H_{\mathbf{x}}} w_{q_1 q_2 \cdots q_M}(|\boldsymbol{\xi}|) \xi_1^{n_1+q_1} \xi_2^{n_2+q_2} \cdots \xi_M^{n_M+q_M} \mathrm{d}V, \tag{6}$$

while the constant vector on the right-hand side of Eq. (5) is given by

$$b_{n_1 n_2 \cdots n_M}^{p_1 p_2 \cdots p_M} = n_1!n_2!\cdots n_M! \delta_{n_1 p_1} \delta_{n_2 p_2} \cdots \delta_{n_M p_M}. \tag{7}$$

According to the concept of the PDDO, the degree of nonlocality can be controlled either by reducing the family size $H_{\mathbf{x}}$ or by increasing the number of terms in the Taylor Series Expansion (TSE). Selecting an optimal horizon size is therefore essential to ensure numerical convergence and maintain acceptable accuracy within a reasonable computational cost. A comprehensive derivation of the peridynamic operators for two-dimensional scalar fields is presented by Dorduncu et al. [48].

4. Field equations of higher-order shear deformation theory

The kinematical formulation of shear-deformable shells can be rigorously deduced from the elasticity solution of the Saint-Venant bending problem, as comprehensively discussed in Faghidian [49]. The displacement field of a laminated composite spherical shell (Fig. 2a) based on the higher-order shear deformation theory is expressed as follows, with Reddy and Liu [50] pioneering the application of the third-order theory to shell structures and Sayyad and Ghugal [51] providing a generalized formulation that can include different higher-order functions:

$$\begin{aligned} u^*(x,y,z) &= \left(1+\frac{z}{R_x}\right) u(x,y) - z\, w_{,x}(x,y) + f(z)\theta_x(x,y), \\ v^*(x,y,z) &= \left(1+\frac{z}{R_y}\right) v(x,y) - z\, w_{,y}(x,y) + f(z)\theta_y(x,y), \\ w^*(x,y,z) &= w(x,y). \end{aligned} \tag{8}$$

In this context, $u^*(x, y, z)$ and $v^*(x, y, z)$ represent the axial displacement field, while $w^*(x, y, z)$ indicates the transverse displacement field of the shell. Here, $u(x, y)$ and $v(x, y)$ are the axial displacements, and $w(x, y)$ is the mid-surface deflection of the shell, with x and y being curvilinear orthogonal coordinates at the mid-surface and z is the

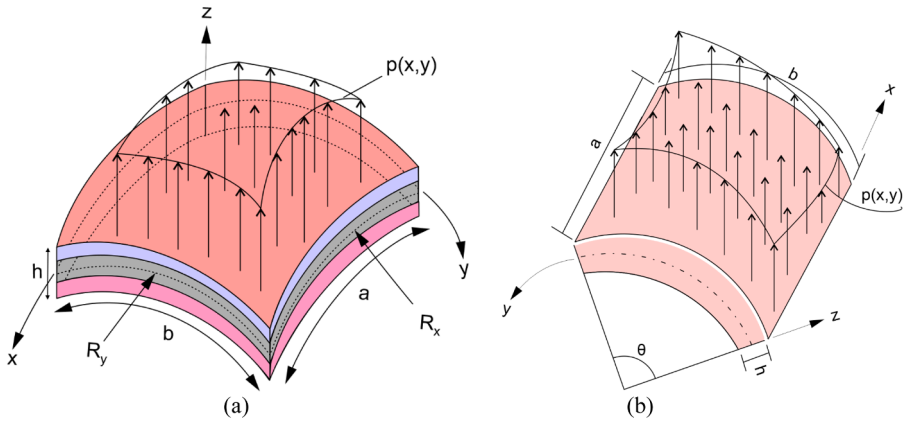

Fig. 2. a) Spherical shell coordinate system, b) Cylindrical shell coordinate system.

coordinate in the shell's thickness direction (Fig. 2b). The section's rotation of a transverse normal about the x-axis is $\theta_y(x,y)$, and about the y-axis is $\theta_x(x,y)$. $R_x$and R_y are the radii of curvature for the spherical shell. In the cylindrical shell case, $R_x = \infty$, so only R_y remains as the curvilinear coordinate, and x becomes a straight axis. Therefore, in Fig. 2b, only y expresses the curvilinear coordinate. Additionally, $f(z)$ is known as the shear function, shaping the stress and strain distribution through the structure's thickness (h). These functions can take polynomial, exponential, or trigonometric forms. In this research, Reddy's [5] shear function $z\left(1-\frac{4z^2}{3h^2}\right)$ is applied to all the examples, due to its ability to satisfy the zero transverse shear stress conditions at the top and bottom surfaces of the shell, and is a widely accepted function for benchmarking in the literature. Furthermore, Bab and Kutlu [8,9] also included Reddy's function in their comparative study of different shear functions for laminated composite plates and shells.

In an orthogonal curvilinear coordinate system, the engineering normal and shear strain components are given as [4]:

$$\varepsilon_i = \frac{\partial}{\partial \xi_i}\left(\frac{u_i}{A_i}\right) + \frac{1}{A_i}\sum_{k=1}^{3}\frac{u_k}{A_k}\frac{\partial A_i}{\partial \xi_k}$$
$$\gamma_{ij} = \frac{1}{A_i A_j}\left[{A_1}^2\frac{\partial}{\partial \xi_j}\left(\frac{u_i}{A_i}\right) + {A_j}^2\frac{\partial}{\partial \xi_i}\left(\frac{u_j}{A_j}\right)\right] \quad (i \neq j), \tag{9}$$

where

$$\xi_3 = \zeta, A_1 = a_1\left(1+\frac{\zeta}{R_1}\right), A_2 = a_2\left(1+\frac{\zeta}{R_2}\right) \tag{10}$$

and a_α ($\alpha = 1, 2$) represents the square root of the surface metric tensor ($g_{\alpha\beta}$ ($\alpha,\beta = 1, 2$)) given as

$$g_{\alpha\beta} = g_\alpha . g_\beta, a_\alpha = \sqrt{g_{\alpha\alpha}}. \tag{11}$$

Eq. (11) shows g_1 and $g_2$as the tangents to the ξ_1 and ξ_2 axes, respectively. Eq. (9) can be reformulated by adapting Reddy's [4] notation to the present framework as follows:

$$\begin{array}{llll} \xi_1 \to x, & u_1 \to u, & \varepsilon_1 \to \varepsilon_{xx}, & \gamma_{12} \to \gamma_{xy}, \\ \xi_2 \to y, & u_2 \to v, & \varepsilon_2 \to \varepsilon_{yy}, & \gamma_{13} \to \gamma_{xz}, \\ \zeta \to z, & u_3 \to w, & \varepsilon_3 \to \varepsilon_{zz}, & \gamma_{23} \to \gamma_{yz}. \end{array} \tag{12}$$

The Eq. (13) summarizes the linear strain components from the above equations:

$$\begin{aligned} \varepsilon_{xx} &= u_{,x} - z\,w_{,xx} + \frac{w}{R_x} + f(z)\theta_{x,x}, \\ \varepsilon_{yy} &= v_{,y} - z\,w_{,yy} + \frac{w}{R_y} + f(z)\theta_{y,y}, \\ \gamma_{xy} &= u^*_{,y} + v^*_{,x} = u_{,y} + v_{,x} - 2z\,w_{,xy} + f(z)\left(\theta_{x,y} + \theta_{y,x}\right), \\ \gamma_{yz} &= v^*_{,z} + w^*_{,y} = f_{,z}(z)\theta_y(x,y), \\ \gamma_{xz} &= u^*_{,z} + w^*_{,x} = f_{,z}(z)\theta_x(x,y). \end{aligned} \tag{13}$$

The stress-strain relations for the k'th layer of the laminated composite shell are given by Hooke's law [2] as follows:

$$\begin{Bmatrix} \sigma_{xx} \\ \sigma_{yy} \\ \sigma_{xy} \\ \sigma_{yz} \\ \sigma_{xz} \end{Bmatrix}^{(k)} = \begin{bmatrix} \overline{Q}_{11} & \overline{Q}_{12} & \overline{Q}_{16} & 0 & 0 \\ \overline{Q}_{12} & \overline{Q}_{22} & \overline{Q}_{26} & 0 & 0 \\ \overline{Q}_{16} & \overline{Q}_{26} & \overline{Q}_{66} & 0 & 0 \\ 0 & 0 & 0 & \overline{Q}_{44} & \overline{Q}_{45} \\ 0 & 0 & 0 & \overline{Q}_{45} & \overline{Q}_{55} \end{bmatrix}^{(k)} \begin{Bmatrix} \varepsilon_{xx} \\ \varepsilon_{yy} \\ \gamma_{xy} \\ \gamma_{yz} \\ \gamma_{xz} \end{Bmatrix}^{(k)}. \tag{14}$$

Herein, $\overline{Q}_{ij}$ represents the transformed and reduced material stiffness coefficients, while $\sigma_{ii}^{(k)}$ and $\sigma_{ij}^{(k)}$represent the normal and shear stress components, respectively, within the kth layer.

4.1. Governing equations for laminated composite shells

To obtain the governing equations of a laminated composite shell according to HSDT, Hamilton's principle [4,52] is revealed as

$$\delta U - \delta V = 0. \tag{15}$$

Here,$\delta U$and δV define the virtual strain energy and virtual work of external loads, respectively. The virtual strain energy of the laminated composite shell is stated through the strain and stress fields:

$$\delta U = \int_A \left(\sigma_{xx}^{(k)}\delta\varepsilon_{xx}^{(k)} + \sigma_{yy}^{(k)}\delta\varepsilon_{yy}^{(k)} + \sigma_{xy}^{(k)}\delta\gamma_{xy}^{(k)} + \sigma_{yz}^{(k)}\delta\gamma_{yz}^{(k)} + \sigma_{xz}^{(k)}\delta\gamma_{xz}^{(k)}\right)\mathrm{d}A. \tag{16}$$

Here corresponds the shell cross-sectional area. Inserting the variation of the strain field from Eq. (13), the expression for the virtual strain energy becomes

$$\delta U = \int_A \begin{pmatrix} N_{xx}\delta u_{,x} + M_{xx,x}\delta w_{,x} + M^f_{xx,x}\delta\theta_{x,x} + N_{yy}\delta v_{,y} + M_{yy,y}\delta w_{,y} + \\ M^f_{yy,y}\delta\theta_{y,y} + N_{xy}\delta u_{,y} + N_{xy}\delta v_{,x} + M_{xy,x}\delta w_{,y} + M_{xy,y}\delta w_{,x} + \\ M^f_{xy}\delta\theta_{x,y} + M^f_{xy}\delta\theta_{y,x} + Q_{yz}\delta\theta_y + Q_{xz}\delta\theta_x + \left(N_{xx}/R_x + N_{yy}/R_y\right)\delta w \end{pmatrix}\mathrm{d}A. \tag{17}$$

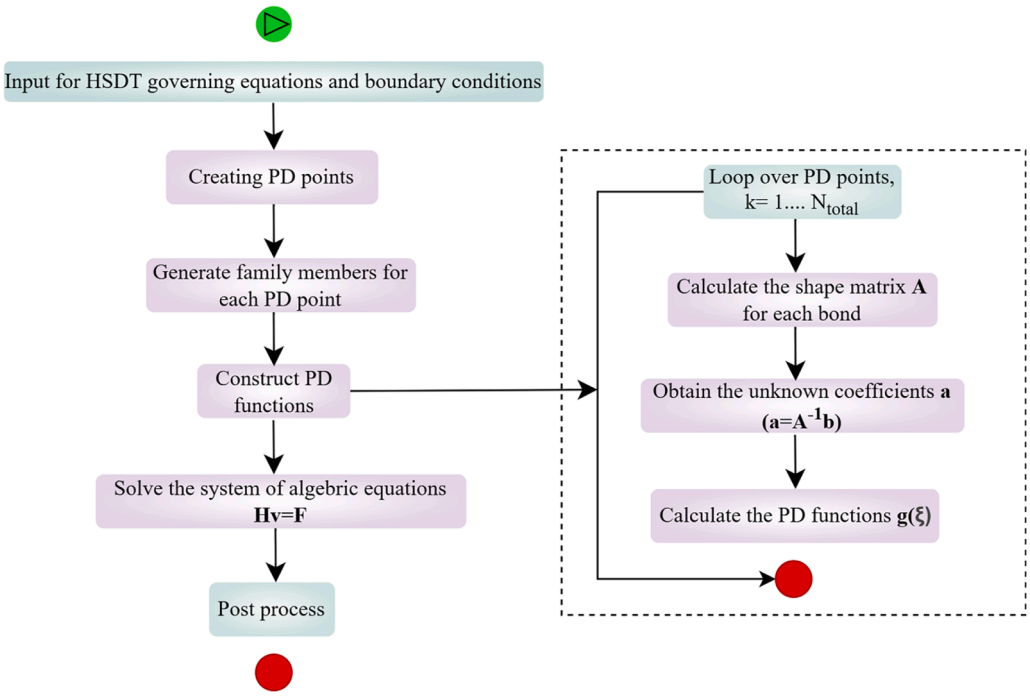

Fig. 3. PDDO flowchart for solving HSDT equilibrium equations.

For the cross-section, normal forces (N_{xx} , N_{yy} , N_{xy}), moments $\left(M_{xx},\ M_{yy},\ M_{xy},\ M^f_{xx},\ M^f_{yy},\ M^f_{xy}\right)$, and shear resultants ($Q_{yz}$, Q_{xz}) appearing in the Eq. (17) are given in terms of the stress integrals as follows:

$$\begin{aligned}
\mathbf{N} &= \{N_{xx}\ \ N_{yy}\ \ N_{xy}\}^T = \int_{-h/2}^{h/2} \{\sigma_{xx}\ \ \sigma_{yy}\ \ \sigma_{xy}\}^T \mathrm{d}z \\
\mathbf{M} &= \{M_{xx}\ \ M_{yy}\ \ M_{xy}\}^T = \int_{-h/2}^{h/2} \{z\sigma_{xx}\ \ z\sigma_{yy}\ \ z\sigma_{xy}\}^T \mathrm{d}z \\
\mathbf{M}^f &= \left\{M^f_{xx}\ \ M^f_{yy}\ \ M^f_{xy}\right\}^T = \int_{-h/2}^{h/2} \{f(z)\sigma_{xx}\ \ f(z)\sigma_{yy}\ \ f(z)\sigma_{xy}\}^T \mathrm{d}z \\
\mathbf{Q} &= \{Q_{yz}\ \ Q_{xz}\}^T = \int_{-h/2}^{h/2} \{f'(z)\sigma_{yz}\ \ f'(z)\sigma_{xz}\}^T \mathrm{d}z.
\end{aligned} \tag{18}$$

Eq. (19) implicitly and Eq. (20) explicitly illustrate the relationship between strain measures and stress resultants through sectional compliance terms (such that $A'_{ij}B'_{ij}..H'_{ij}A'^s_{ij}$), which are the inverses of ($\mathbf{S} = \mathbf{C}^{-1}$) sectional stiffness terms $\left(A_{ij}\ B_{ij}\ ..\ H_{ij}\ A^s_{ij}\right)$.

$$\mathbf{e^P} = \mathbf{SP} \text{ or } \begin{Bmatrix} \boldsymbol{\varepsilon}_m \\ \boldsymbol{\kappa}_0 \\ \boldsymbol{\kappa}_1 \\ \boldsymbol{\varepsilon}_s \end{Bmatrix} = \begin{bmatrix} \mathbf{A}' & \mathbf{B}' & \mathbf{E}' & \mathbf{0} \\ \mathbf{B}' & \mathbf{D}' & \mathbf{F}' & \mathbf{0} \\ \mathbf{E}' & \mathbf{F}' & \mathbf{H}' & \mathbf{0} \\ \mathbf{0} & \mathbf{0} & \mathbf{0} & \mathbf{A}'^s \end{bmatrix} \begin{Bmatrix} \mathbf{N} \\ \mathbf{M} \\ \mathbf{M}^f \\ \mathbf{Q} \end{Bmatrix}, \tag{19}$$

$$\begin{Bmatrix} u_{,x} + w/R_x \\ v_{,y} + w/R_y \\ u_{,y} + v_{,x} \\ -w_{,xx} \\ -w_{,yy} \\ -2w_{,xy} \\ \theta_{x,x} \\ \theta_{y,y} \\ \theta_{x,y} + \theta_{y,x} \\ \theta_y \\ \theta_x \end{Bmatrix} = \begin{bmatrix} A'_{11} & A'_{12} & A'_{16} & B'_{11} & B'_{12} & B'_{16} & E'_{11} & E'_{12} & E'_{16} & 0 & 0 \\ A'_{12} & A'_{22} & A'_{26} & B'_{12} & B'_{22} & B'_{26} & E'_{12} & E'_{22} & E'_{26} & 0 & 0 \\ A'_{16} & A'_{26} & A'_{66} & B'_{16} & B'_{26} & B'_{66} & E'_{16} & E'_{26} & E'_{66} & 0 & 0 \\ B'_{11} & B'_{12} & B'_{16} & D'_{11} & D'_{12} & D'_{16} & F'_{11} & F'_{12} & F'_{16} & 0 & 0 \\ B'_{12} & B'_{22} & B'_{26} & D'_{12} & D'_{22} & D'_{26} & F'_{12} & F'_{22} & F'_{26} & 0 & 0 \\ B'_{16} & B'_{26} & B'_{66} & D'_{16} & D'_{26} & D'_{66} & F'_{16} & F'_{26} & F'_{66} & 0 & 0 \\ E'_{11} & E'_{12} & E'_{16} & F'_{11} & F'_{12} & F'_{16} & H'_{11} & H'_{12} & H'_{16} & 0 & 0 \\ E'_{12} & E'_{22} & E'_{26} & F'_{12} & F'_{22} & F'_{26} & H'_{12} & H'_{22} & H'_{26} & 0 & 0 \\ E'_{16} & E'_{26} & E'_{66} & F'_{16} & F'_{26} & F'_{66} & H'_{16} & H'_{26} & H'_{66} & 0 & 0 \\ 0 & 0 & 0 & 0 & 0 & 0 & 0 & 0 & 0 & A'^s_{44} & A'^s_{45} \\ 0 & 0 & 0 & 0 & 0 & 0 & 0 & 0 & 0 & A'^s_{45} & A'^s_{55} \end{bmatrix} \begin{Bmatrix} N_{xx} \\ N_{yy} \\ N_{xy} \\ M_{xx} \\ M_{yy} \\ M_{xy} \\ M^f_{xx} \\ M^f_{yy} \\ M^f_{xy} \\ Q_{yz} \\ Q_{xz} \end{Bmatrix}, \tag{20}$$

in which the sectional rigidity terms are calculated as follows:

$$\left.\begin{aligned}\left(A_{ij}\quad B_{ij}\quad D_{ij}\right)&=\sum_{k=1}^{N}\int_{z_{(k-1)}}^{z_{(k)}}\overline{Q}_{ij}^{(k)}\left(1\quad z\quad z^2\right)\mathrm{d}z\\ \left(E_{ij}\quad F_{ij}\quad H_{ij}\right)&=\sum_{k=1}^{N}\int_{z_{(k-1)}}^{z_{(k)}}\overline{Q}_{ij}^{(k)}\left(f(z)\quad zf(z)\quad f(z)^2\right)\mathrm{d}z\end{aligned}\right\};\quad i,j=1,2,6$$

$$A_{ij}^{s}=\sum_{k=1}^{N}\int_{z_{(k-1)}}^{z_{(k)}}\overline{Q}_{ij}^{(k)}(f'(z))^2\mathrm{d}z\quad;\quad i,j=4,5\,. \tag{21}$$

Hence, the virtual strain energy of the laminated composite shell is indicated by

$$\delta U=\int_{A}\delta\boldsymbol{\varepsilon}^{T}\mathbf{D}\varepsilon\mathrm{d}A. \tag{22}$$

Consequently, the virtual work done by the distributed load $q(x, y)$ is stated as:

$$\delta V=\int_{A}q(x,y)\delta w\mathrm{d}A. \tag{23}$$

Applying Eqs. (17) and (23), the Hamilton principle (15) generates the motion equations for the laminated shell based on HSDT:

$$\begin{aligned}&q_x+N_{xx,x}+N_{xy,y}=0\quad;\quad q_y+N_{xy,x}+N_{yy,y}=0,\\ &q_z+M_{xx,xx}+M_{yy,yy}+2M_{xy,xy}-\frac{N_{xx}}{R_x}-\frac{N_{yy}}{R_y}=0,\\ &M_{xx}^{f},x+M_{xy}^{f},y-Q_{xz}=0\quad;\quad M_{yy}^{f},y+M_{xy}^{f},x-Q_{yz}=0\,.\end{aligned} \tag{24}$$

Finally, the boundary conditions for the laminated shell based on HSDT are derived from the Euler-Lagrange equations:

$$\begin{aligned}&N_{xx}n_x+N_{xy}n_y=0 && \text{or } \delta u=0,\\ &N_{xy}n_x+N_{yy}n_y=0 && \text{or } \delta v=0,\\ &M_{xx,x}n_x+M_{yy,y}n_y+2M_{xy,x}n_y=0 && \text{or } \delta w=0,\\ &M_{xx}^{f}n_x+M_{xy}^{f}n_y=0 && \text{or } \delta\theta_x=0,\\ &M_{xy}^{f}n_x+M_{yy}^{f}n_y=0 && \text{or } \delta\theta_y=0\,.\end{aligned} \tag{25}$$

The equilibrium equations, using the kinematic and constitutive relations, take the form

$$\begin{aligned}&\delta u: A_{11}u_{,xx}+2A_{16}u_{,xy}+A_{66}u_{,yy}+A_{12}v_{,xy}+A_{16}v_{,xx}+A_{26}v_{,yy}+A_{66}v_{,xy}+E_{11}\theta_{x,xx}\\ &+2E_{16}\theta_{x,xy}+E_{66}\theta_{x,yy}+E_{12}\theta_{y,xy}+E_{16}\theta_{y,xx}+E_{26}\theta_{y,yy}+E_{66}\theta_{y,xy}-B_{11}w_{,xxx}\\ &-B_{12}w_{,xyy}-3B_{16}w_{,xxy}-B_{26}w_{,yyy}-2B_{66}w_{,xyy}+A_{11}\frac{w_{,x}}{R_x}+A_{12}\frac{w_{,x}}{R_y}+A_{16}\frac{w_{,y}}{R_x}+A_{26}\frac{w_{,y}}{R_y}=0,\\ &\delta v: A_{16}u_{,xx}+A_{66}u_{,xy}+A_{12}u_{,xy}+A_{26}u_{,yy}+2A_{26}v_{,xy}+A_{66}v_{,xx}+A_{22}v_{,yy}+E_{16}\theta_{x,xx}\\ &+E_{66}\theta_{x,xy}+E_{12}\theta_{x,xy}+E_{26}\theta_{x,yy}+E_{26}\theta_{y,xy}+E_{66}\theta_{y,xx}+E_{22}\theta_{y,yy}+E_{26}\theta_{y,xy}-B_{12}w_{,xxy}\\ &-B_{16}w_{,xxx}-2B_{66}w_{,xxy}-B_{22}w_{,yyy}-3B_{26}w_{,xyy}+A_{16}\frac{w_{,x}}{R_x}+A_{26}\frac{w_{,x}}{R_y}+A_{12}\frac{w_{,y}}{R_x}+A_{22}\frac{w_{,y}}{R_y}=0,\\ &\delta w: B_{11}u_{,xxx}+3B_{16}u_{,xxy}+B_{12}u_{,xyy}+B_{26}u_{,yyy}+2B_{66}u_{,xyy}+(B_{12}+2B_{66})v_{,xxy}+B_{16}v_{,xxx}+\\ &B_{22}v_{,yyy}+3B_{26}v_{,xyy}+F_{11}\theta_{x,xxx}+3F_{16}\theta_{x,xxy}+(F_{12}+2F_{66})\theta_{x,xyy}+(F_{12}+2F_{66})\theta_{y,xxy}+\\ &F_{26}\theta_{x,yyy}+F_{16}\theta_{y,xxx}+F_{22}\theta_{y,yyy}+3F_{26}\theta_{y,xyy}-D_{11}w_{,xxxx}-(2D_{12}+4D_{66})w_{,xxyy}-4D_{16}w_{,xxxy}\\ &-D_{22}w_{,yyyy}-4D_{26}w_{,xyyy}+B_{11}\frac{w_{,xx}}{R_x}+B_{12}\frac{w_{,xx}}{R_y}+B_{12}\frac{w_{,yy}}{R_x}+B_{22}\frac{w_{,yy}}{R_y}+2B_{16}\frac{w_{,xy}}{R_x}+2B_{26}\frac{w_{,xy}}{R_y}\\ &+p-\left(\begin{array}{l}\left(\begin{array}{l}A_{11}u_{,x}-B_{11}w_{,xx}+E_{11}\theta_{x,x}+A_{11}\frac{w}{R_x}+A_{12}v_{,y}-B_{12}w_{,yy}+E_{12}\theta_{y,y}+A_{12}\frac{w}{R_y}\\ +A_{16}u_{,y}+A_{16}v_{,x}-2B_{16}w_{,xy}+E_{16}\left(\theta_{x,y}+\theta_{y,x}\right)\end{array}\right)\frac{1}{R_x}\\ \left(\begin{array}{l}A_{12}u_{,x}-B_{12}w_{,xx}+E_{12}\theta_{x,x}+A_{12}\frac{w}{R_x}+A_{22}v_{,y}-B_{22}w_{,yy}+E_{22}\theta_{y,y}+A_{22}\frac{w}{R_y}\\ +A_{26}u_{,y}+A_{26}v_{,x}-2B_{26}w_{,xy}+E_{26}\left(\theta_{x,y}+\theta_{y,x}\right)\end{array}\right)\frac{1}{R_y}\end{array}\right)=0,\\ &\delta\theta_x: E_{11}u_{,xx}+2E_{16}u_{,xy}+E_{66}u_{,yy}+E_{12}v_{,xy}+E_{16}v_{,xx}+E_{26}v_{,yy}+E_{66}v_{,xy}+H_{11}\theta_{x,xx}+\\ &2H_{16}\theta_{x,xy}+H_{66}\theta_{x,yy}-A_{55}^{s}\theta_x+H_{12}\theta_{y,xy}+H_{16}\theta_{y,xx}+H_{26}\theta_{y,yy}+H_{66}\theta_{y,xy}-A_{45}^{s}\theta_y\\ &-F_{11}w_{,xxx}-F_{12}w_{,xyy}-3F_{16}zw_{,xxy}-F_{26}w_{,yyy}-2F_{66}w_{,xyy}+E_{11}\frac{w_{,x}}{R_x}+E_{12}\frac{w_{,x}}{R_y}+E_{16}\frac{w_{,y}}{R_x}+E_{26}\frac{w_{,y}}{R_y}=0,\\ &\delta\theta_y: E_{16}u_{,xx}+(E_{12}+E_{66})u_{,xy}+E_{26}u_{,yy}+2E_{26}v_{,xy}+E_{66}v_{,xx}+E_{22}v_{,yy}+H_{16}\theta_{x,xx}+\\ &(H_{66}+H_{12})\theta_{x,xy}+H_{26}\theta_{x,yy}-A_{45}^{s}\theta_x+2H_{26}\theta_{y,xy}+H_{66}\theta_{y,xx}+H_{22}\theta_{y,yy}-A_{44}^{s}\theta_y-F_{16}w_{,xxx}-3F_{26}w_{,xyy}\\ &-2F_{66}w_{,xxy}-F_{12}w_{,xxy}-F_{22}w_{,yyy}+E_{16}\frac{w_{,x}}{R_x}+E_{26}\frac{w_{,x}}{R_y}+E_{22}\frac{w_{,y}}{R_y}+E_{12}\frac{w_{,y}}{R_x}=0\,.\end{aligned} \tag{26}$$

Table 1
Mechanical properties of materials used in the examples, including Young's moduli, E_i, and shear moduli G_{ij}, with $i, j = 1 - 3$.

Engineering Constants	Materials	
	A	B
E_1	25 [GPa]	132.38 [GPa]
E_2	1 [GPa]	10.76 [GPa]
E_3	1 [GPa]	10.76 [GPa]
υ_{12}	0.25	0.24
υ_{13}	0.25	0.24
υ_{23}	0.25	0.49
G_{12}	0.5 [GPa]	5.65 [GPa]
G_{13}	0.5 [GPa]	5.65 [GPa]
G_{23}	0.2 [GPa]	3.61 [GPa]

Utilizing Madenci et al. [39], up to forth-order derivatives in Eq. (26) are reformulated in terms of their corresponding nonlocal representations within the PD theory as:

$$\frac{\partial^{p_1+p_2}}{\partial x^{p_1}\partial y^{p_2}} f(x_{(k)}, y_{(k)}) = \sum_{j=1}^{N_{(k)}} \left(f\left(x_{(j)}, y_{(j)}\right) - f(x_{(k)}, y_{(k)}) \right) g_4^{p_1 p_2}\left(\boldsymbol{\xi}_{(k)(j)}\right) A_{(j)} \quad (27)$$

where $g_4^{p_1 p_2}\left(\boldsymbol{\xi}_{(k)(j)}\right)$ denotes the PD function defined according to Eq. (1). The term $A_{(j)} = \Delta x \Delta y$ corresponds to the area associated with PD point j. The indices $p_1$and p_2, each taking values between 0 to 4, indicate the order of the partial differentiation with respect to the spatial coordinates x and y, respectively. The field variable $f(x_{(k)},y_{(k)})$ represents the displacement components used in the HSDT, namely u , v , w , θ_x , θ_y.

4.2. Calculation of transverse shear stress distributions

Accurate calculation of transverse shear stress in laminated shells is essential to prevent issues like delamination. Applying Hooke's law (Eq. (14)) often results in discontinuous shear stress distributions at material interfaces and on free surfaces. To get more realistic stress distributions, equilibrium equations from elasticity theory [53] are utilized:

$$\tau_{xz} = -\int_{-h}^{z} \left(\sigma_{xx,x} + \sigma_{xy,y}\right) \mathrm{d}\bar{z}, \quad (28)$$

$$\tau_{yz} = -\int_{-h}^{z} \left(\sigma_{xy,x} + \sigma_{yy,y}\right) \mathrm{d}\bar{z}, \quad (29)$$

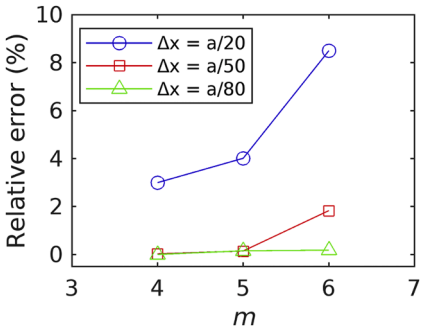

Fig. 4. Relative error (%) of the deflection for 0°/90°/90°/0° lamination and $R/a = 5$ under sinusoidal loading.

where $\bar{z}$ is a dummy variable for integral calculation. This approach ensures a more accurate representation of shear stresses across layers, thereby enhancing the reliability of the stress analysis in laminated composite shells.

At each layer of the shell, the first-order spatial derivatives of the axial and in-plane stress components are expressed through their corresponding PD formulations as follows [39]:

$$\frac{\partial}{\partial x}\sigma_{xx}(x_{(k)}, y_{(k)}) = \sum_{j=1}^{N_{(k)}} \left(\sigma_{xx}\left(x_{(j)}, y_{(j)}\right) - \sigma_{xx}(x_{(k)}, y_{(k)})\right) g_1^{10}\left(\boldsymbol{\xi}_{(k)(j)}\right) A_{(j)}, \quad (30)$$

$$\frac{\partial}{\partial y}\sigma_{yy}(x_{(k)}, y_{(k)}) = \sum_{j=1}^{N_{(k)}} \left(\sigma_{yy}\left(x_{(j)}, y_{(j)}\right) - \sigma_{yy}(x_{(k)}, y_{(k)})\right) g_1^{01}\left(\boldsymbol{\xi}_{(k)(j)}\right) A_{(j)}, \quad (31)$$

$$\frac{\partial}{\partial x}\sigma_{xy}(x_{(k)}, y_{(k)}) = \sum_{j=1}^{N_{(k)}} \left(\sigma_{xy}\left(x_{(j)}, y_{(j)}\right) - \sigma_{xy}(x_{(k)}, y_{(k)})\right) g_1^{10}\left(\boldsymbol{\xi}_{(k)(j)}\right) A_{(j)}, \quad (32)$$

$$\frac{\partial}{\partial y}\sigma_{xy}(x_{(k)}, y_{(k)}) = \sum_{j=1}^{N_{(k)}} \left(\sigma_{xy}\left(x_{(j)}, y_{(j)}\right) - \sigma_{xy}(x_{(k)}, y_{(k)})\right) g_1^{01}\left(\boldsymbol{\xi}_{(k)(j)}\right) A_{(j)}. \quad (33)$$

Fig. 3 presents the flowchart illustrating the implementation of PDDO for solving the HSDT equilibrium equations and applying the boundary conditions, which is composed of PDDO from Sections 2-3, HSDT from Section 4, and the numerical implementation from Dorduncu et al. [48].

Table 2
Non-dimensional cross-ply spherical shell center deflection under sinusoidal loading.

Theory	R/a	Cross-ply			Relative error (%)		
		0°/90°	0°/90°/0°	0°/90°/90°/0°	0°/90°	0°/90°/0°	0°/90°/90°/0°
PD-HSDT (Present)	5	11.0779	6.7510	6.7834	0.79	0.26	0.05
FSDT (Reddy and Liu)		11.429	6.4253	6.3623	2.36	5.07	6.25
HSDT (Reddy and Liu)		11.166	6.7688	6.7865			
PD-HSDT (Present)	10	11.7985	7.0136	7.0508	0.82	0.27	0.04
FSDT (Reddy and Liu)		12.123	6.6247	6.5595	1.91	5.80	7.00
HSDT (Reddy and Liu)		11.896	7.0325	7.0536			
PD-HSDT (Present)	20	11.9887	7.0825	7.1209	0.87	0.27	0.04
FSDT (Reddy and Liu)		12.309	6.6756	6.6099	1.78	6.00	7.21
HSDT (Reddy and Liu)		12.094	7.1016	7.1237			
PD-HSDT (Present)	50	12.1317	7.1021	7.1408	0.15	0.27	0.04
FSDT (Reddy and Liu)		12.362	6.6902	6.6244	1.74	6.05	7.27
HSDT (Reddy and Liu)		12.150	7.1212	7.1436			
PD-HSDT (Present)	100	12.0474	7.1049	7.1437	0.91	0.27	0.04
FSDT (Reddy and Liu)		12.370	6.6923	6.6264	1.74	6.06	7.28
HSDT (Reddy and Liu)		12.158	7.1240	7.1464			

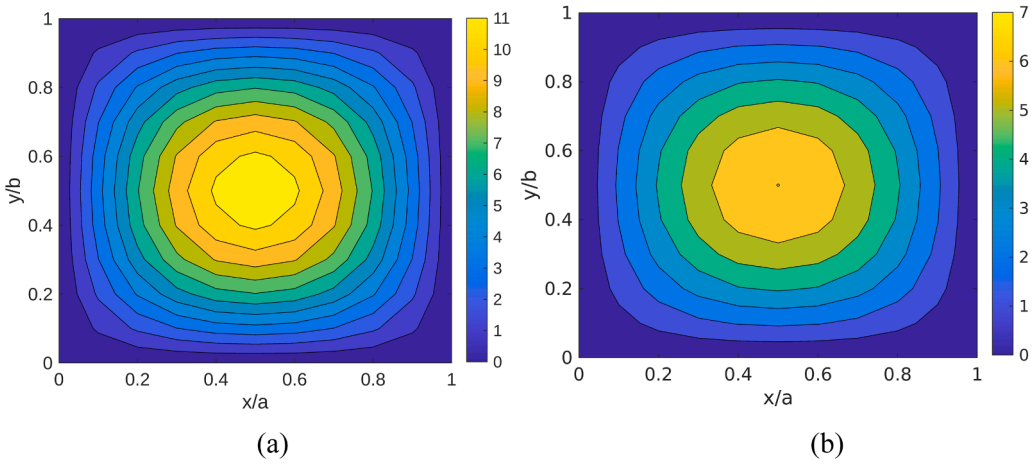

Fig. 5. Non-dimensional deflection distribution along $x-y$ surface for $R/a = 10$ and $a/h = 10$a) 0°/90° lamination b) 0°/90°/0° lamination.

5. Numerical examples

To evaluate the accuracy and computational performance of the proposed PD-HSDT formulation, several numerical studies are performed under static loading conditions with particular emphasis on displacement fields and stress resultants. The numerical solutions are obtained using a Fortran-based program developed by the authors. To validate the proposed formulation and implementation, results are compared with the exact HSDT solutions by Reddy and Liu [54], analytical results by Khdeir et al. [55], and closed-form solutions from Sayyad and Ghugal's generalized higher-order theory [51]. The analysis includes various loading and boundary conditions. Uniform and sinusoidal loads are adopted as they sufficiently represent both overall and localized structural responses, while also enabling straightforward validation against existing literature. Two different materials are considered with their elastic properties summarized in Table 1. These materials, referred to as A and B, represent anisotropic composites with directional mechanical properties and are commonly used and compared in the literature, enabling a comparative analysis of how variations in stiffness, shear, and Poisson characteristics affect the bending response of laminated shell structures.

5.1. Simply Supported cross-ply spherical shells under sinusoidal loading

Cross-ply (0°/90°, 0°/90°/0°, and 0°/90°/90°/0°) laminated spherical shells are analyzed based on the geometric conditions shown in Fig. 1a, where a and b represent the arc lengths of the shell in the x and y directions, respectively, with $a = b = 1$. The shells are under the influence of a transverse load of function $p(x, y) = p_0 \sin(\pi x/a)\sin(\pi y/b)$ distributed over their outer surface. The curvatures in the spherical shell are denoted as $R_x = R_y = R$. Each layer of equal thickness is considered to be formed with material A. The $\rho = a/h = 10$ is considered the shell length-thickness ratio. The boundary conditions in this example are simply supported along all four edges (SSSS) and are defined based on Eq. (25), which imposes zero transverse displacement and bending moments at the boundaries. This formulation ensures that the plate edges can freely rotate while preventing out-of-plane deflections, thereby satisfying both the mathematical structure and the physical interpretation of simply supported conditions, as detailed below [4]:

Table 4
Non-dimensional symmetrical spherical shell deflection and stresses under sinusoidal loading.

R/a	Theory	$\overline{w}$	$\overline{\sigma}_{xx}$	$\overline{\sigma}_{yy}$	$\overline{\tau}_{yz}$	$\overline{\tau}_{xz}$
5	Sayyad & Ghugal	0.6769	0.5218	0.0352	0.1109	0.3508
	PD-HSDT	0.6772	0.5251	0.0352	0.1094	0.3642
10	Sayyad & Ghugal	0.7032	0.5515	0.0374	0.1152	0.3645
	PD-HSDT	0.7037	0.5551	0.0374	0.1137	0.3784
20	Sayyad & Ghugal	0.7102	0.5617	0.0381	0.1163	0.3681
	PD-HSDT	0.7106	0.5653	0.0382	0.1148	0.3821
50	Sayyad & Ghugal	0.7121	0.5662	0.0385	0.1167	0.3691
	PD-HSDT	0.7126	0.5698	0.0385	0.1151	0.3832
100	Sayyad & Ghugal	0.7124	0.5674	0.0386	0.1167	0.3692
	PD-HSDT	0.7128	0.5710	0.0386	0.1152	0.3833

Table 3
Non-dimensional cross-ply spherical shell center deflection under uniform loading.

Theory	R/a	Cross-ply			Relative error (%)		
		0°/90°	0°/90°/0°	0°/90°/90°/0°	0°/90°	0°/90°/0°	0/90°/90°/0°
PD-HSDT (Present)	5	17.5640	10.2315	10.6202	0.01	0.97	1.38
FSDT (Reddy and Liu)		19.944	9.794	9.825	13.54	5.21	6.21
HSDT (Reddy and Liu)		17.566	10.332	10.476			
PD-HSDT (Present)	10	18.7167	10.6481	11.0573	0.15	0.97	1.41
FSDT (Reddy and Liu)		19.065	10.110	10.141	1.71	5.97	7.00
HSDT (Reddy and Liu)		18.744	10.752	10.904			
PD-HSDT (Present)	20	19.0165	10.7574	11.1720	0.25	0.96	1.41
FSDT (Reddy and Liu)		19.365	10.191	10.222	1.58	6.18	7.22
HSDT (Reddy and Liu)		19.064	10.862	11.017			
PD-HSDT (Present)	50	19.2539	10.7884	11.2046	0.52	0.96	1.41
FSDT (Reddy and Liu)		19.452	10.214	10.245	1.55	6.23	7.28
HSDT (Reddy and Liu)		19.155	10.893	11.049			
PD-HSDT (Present)	100	19.1048	10.7929	11.2092	0.33	0.96	1.41
FSDT (Reddy and Liu)		19.469	10.218	10.294	1.54	6.24	6.87
HSDT (Reddy and Liu)		19.172	10.898	11.053			

$$\begin{aligned} x = 0,\ a \quad & v = w = \theta_y = N_{xx} = M_{xx} = M^f_{xx} = 0. \\ y = 0,\ b \quad & u = w = \theta_x = N_{yy} = M_{yy} = M^f_{yy} = 0. \end{aligned} \tag{34}$$

To evaluate the results presented in Table 2 in a general structure, the non-dimensional form is carried out according to Eq. (35) for $\alpha = -10^3$.

$$\overline{w} = \frac{\alpha E_2 h^3 w(a/2, b/2)}{p_0 a^4} . \tag{35}$$

To ensure computational efficiency while maintaining solution accuracy, a convergence study is carried out to identify the optimal combination of horizon size ($\delta = m\Delta$) and grid spacing (Δ). As illustrated in Fig. 4, the PDDO solutions exhibit convergence toward the corresponding analytical solution as both δ and Δ are reduced. This behavior aligns with the theoretical basis of nonlocal formulations, where decreasing δ and refining Δ improve the accuracy of stress and strain predictions. For instance, for a fixed horizon ratio $m = \delta/\Delta = 4$, the use of $\Delta x = \Delta y = a/80$ and $a/50$ results in relative differences of only 0.0287 % and 0.0041 %, respectively, compared to the analytical solution. These small discrepancies confirm that sufficient convergence is achieved. Therefore, in the present study, the combination of $\delta = 4\Delta$ and $\Delta x = \Delta y = a/50$ is considered optimal, offering a balance between computational cost and solution fidelity.

According to Table 2, the PD-HSDT results are in good agreement with the exact HSDT solutions of Reddy and Liu [41] and provide more converged values compared to the exact FSDT of Reddy and Liu [41]. The relative error between the present values and the exact HSDT, as well as between the exact FSDT and the exact HSDT, can also be observed in Table 2. The most converged results (0.05 % difference) are obtained for the 0°/90°/90°/0° lamination.

The contour plots above (Fig. 5) visualize the deflection of two laminated composite shells with the same loading and BC's. The left plot shows a 0°/90° stacking sequence, while the right shows a 0°/90°/0° sequence. The x/a and y/b axes represent normalized shell coordinates, and the color scale and contours display normalized deflection values. The maximum normalized deflection observed in the 0°/90° laminated shell is approximately 11 units, while for the 0°/90°/0° laminated shell, it is about 7 units. For both laminations, the maximum deflection is concentrated in the central region of the shell. The shape of the contour lines explains that the shell exhibits more noticeable bending in the center under loading. In the 0°/90° laminate configuration, the deflection distribution exhibits denser contour gradients concentrated around the center, indicating a broader but less localized deformation pattern. In contrast, the 0°/90°/0° laminate shows a more concentrated deflection peak at the center, suggesting enhanced resistance to bending. The inclusion of the 0° layer significantly increases the flexural stiffness of the laminate, resulting in reduced overall deflection and a more confined deformation profile.

5.2. Simply supported cross-ply spherical shells under uniform loading

In this problem, the same shell geometry, length the thickness ratio and boundary conditions as presented in Section 5.1 are considered; however, the structure is now subjected to a uniform ($p(x, y) = p_0$) transverse loading instead of the previously applied load type. The non-dimensional form is also followed by Eq. (35) for $\alpha = -10^3$.

According to Table 3, all the deflection values obtained from the current PD-HSDT are highly compatible with the reference exact HSDT solutions of Reddy and Liu. The relative error between PD-HSDT and exact HSDT decreases as the R/a ratio decreases for 0°/90° and 0/90°/90°/0° laminations. On the other hand, the difference remains almost the same for the 0°/90°/0° lamination across various R/a ratios.

5.3. Symmetric spherical shells with simply supported conditions under sinusoidal loading

In this example, material A from Table 1 is selected to evaluate the deflection and stress responses of spherical shells with a 0°/90°/0° lamination scheme, considering various R/a ratios. The results are compared with the closed-form solutions derived from the generalized higher-order theory proposed by Sayyad and Ghugal [51] under simply supported boundary conditions. The $\rho = a/h = 10$ is considered as the shell length-thickness ratio. The comparisons are made based on the Parabolic Shear Deformation Theory (PSDT) described by Sayyad and Ghugal [51], which corresponds the Reddy's third-order shear deformation theory. The non-dimensional form in terms of deflection, normal, and transverse shear stresses is given in their publication [51].

As seen in Table 4, the present PD-HSDT solutions are consistent with the reference results of Sayyad and Ghugal in terms of both deflection and stress values. The smallest percentage differences are observed for deflection ($\overline{w}$) and normal stress ($\overline{\sigma}_{yy}$) values. Examining the distribution of $\overline{\sigma}_{xx}$at ($a/2$, $b/2$, z/h) through the thickness for different R/a values reveals variations near the top and the bottom surfaces of the shell, especially for lower R/a ratios (Fig. 6a). This behavior can be attributed to the curvature-induced effects and the laminate's stacking sequence, which together influence the bending stress distribution across the thickness. In contrast, the distribution of $\overline{\sigma}_{yy}$ at ($a/2$, $b/2$, z/h) through the thickness shows noticeable differences near the mid-plane of the section depending on the R/a ratio (Fig. 6b). These differences are particularly evident in the central 90° ply when R/a is small, i.e., when

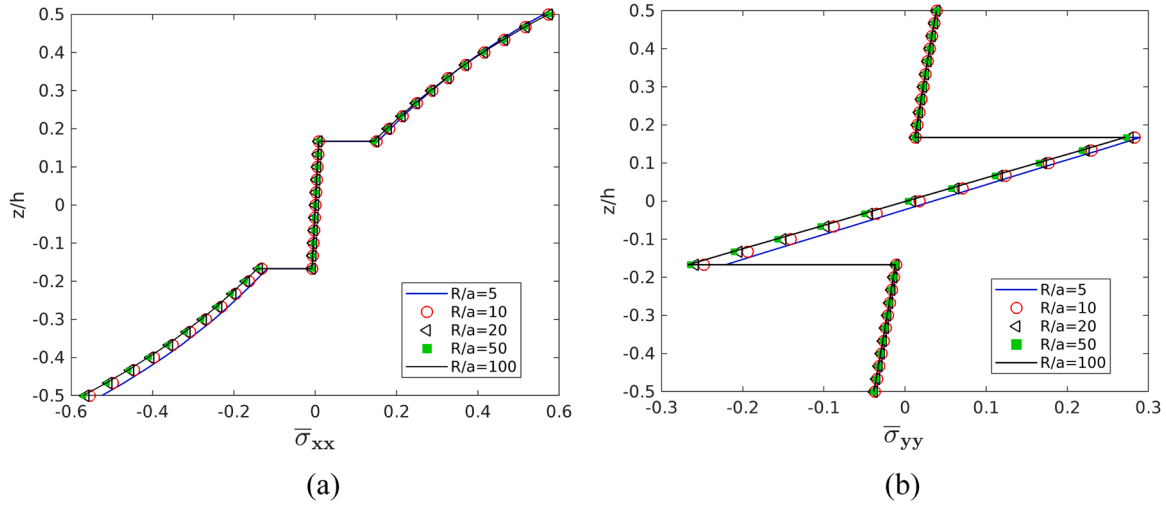

Fig. 6. Non-dimensional normal stress distributions along the normalized thickness (z/h) of the laminated composite shell a) $\overline{\sigma}_{xx}$b) $\overline{\sigma}_{yy}$.

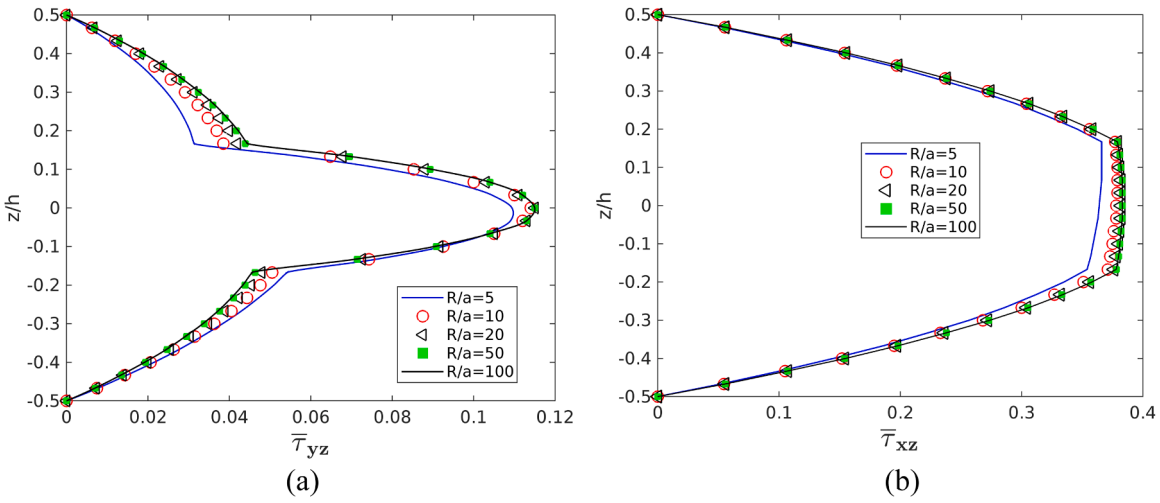

Fig. 7. Non-dimensional transverse shear stress distributions along the normalized thickness (z/h) of the laminated composite shell a) $\overline{\tau}_{yz}$b) $\overline{\tau}_{xz}$.

the curvature is more pronounced. The increased curvature introduces an asymmetry in the stress distribution, leading to a shift where the stress is higher at $h/3$ and lower at -$h/3$ within the 90° layer. In both the current PD-HSDT solution and the reference solution, transverse shear stresses are calculated as explained in Section 4.2. The results ensure interlaminar continuity, as shown in Fig. 7a for $\overline{\tau}_{yz}$ at ($a/2$, 0, z/h) and Fig. 7b for $\overline{\tau}_{xz}$ at (0, $b/2$, z/h). For both stress distributions presented in Figs. 6 and 7, increasing the R/a ratio—indicating a transition from shell-like to plate-like behavior—results in more symmetric profiles through the thickness. However, the transverse shear stress distributions in Fig. 7 are more sensitive to curvature effects compared to the normal stresses in Fig. 6. This is because transverse shear stresses are strongly influenced by the shell's curvature, which alters the orientation of the material sections and amplifies the contribution of shear deformation. Even in symmetric laminates such as 0°/90°/0°, the through-thickness variation of transverse shear stresses becomes asymmetric when curvature is high, primarily due to the non-uniform rotation along the thickness and the resulting shear strain gradients. As a result, the symmetry of shear stress profiles is more severely disrupted in curved geometries than that of the normal stresses.

5.4. Symmetric spherical and doubly-curved shells with various boundary conditions under sinusoidal loading

In this example, the material is selected as B from Table 1, the deflection values of spherical shells are obtained for 0°/90°/0° lamination under various R/aratios, and the results are compared to the analytical HSDT solution of Khdeir et al. [55] under mixed boundary conditions (SCSC). According to the SCSC boundary condition, the two edges of the shell in the x-axis direction are simply supported, while the other two edges in they-axis direction are clamped. In this condition, the edges along the x-axis allow rotation but restrict transverse displacement and bending moment, while the edges along the y-axis prevent both displacement and rotation. These conditions physically represent a shell with differing edge restraints and are mathematically expressed through constraints on displacement and its derivatives within the HSDT framework, as presented below [4].

$$\begin{aligned} x = 0,\ a \quad & u = v = w = w_{,x} = \theta_x = \theta_y = 0. \\ y = 0,\ b \quad & u = w = \theta_x = N_{yy} = M_{yy} = M^f_{yy} = 0. \end{aligned} \tag{36}$$

The $\rho = a/h = 10$ is considered as the shell length-thickness ratio. The non-dimensional form is carried out according to Eq. (35) for $\alpha = 10^2$.

According to Table 5, the present results are compatible with the analytical HSDT of Khdeir et al. [55] and converge more closely than the analytical FSDT values of Khdeir et al. values. The relative errors increase with the increasing R/a ratio for both PD-HSDT and FSDT values.

In this section, all properties remain identical to those of the spherical shell, with the sole variation being the geometry, which is represented by a doubly-curved shell in two configurations: the first configuration with $R_x/a = 10$ and $R_y/a = 5$, and the second configuration with$R_x/a = 10$ and $R_y/a = 20$. Furthermore, the simply supported (SSSS) boundary condition is incorporated.

Upon examination of Table 6, it is evident that the PD-HSDT formulation yields significantly improved results compared to the exact FSDT across all support and curvature conditions, demonstrating closer agreement with the exact HSDT. Furthermore, for both support conditions where $R_y/a = 5$, the PD-HSDT results exhibit a higher degree of accuracy relative to the exact HSDT than in cases where $R_y/a = 20$.

5.5. Symmetric cylindrical shell with various boundary conditions under sinusoidal loading

This example employs the same material properties, loading conditions, boundary constraints, and non-dimensional parameters as Example 5.4. The sole distinction is in the geometry, which is cylindrical herein. Specifically, the curvature of the cylindrical shell is oriented along the axial direction, such that $R_x = \infty$.

In Table 7, the non-dimensional deflection values are compared to

Table 5
Non-dimensional symmetrical spherical shell center deflection under sinusoidal loading.

BC'S	R/a	PD-HSDT (Present)	Analytical FSDT (Khdeir et al.)	Analytical HSDT (Khdeir et al.)	Relative error (%)	
					PD-HSDT	FSDT
SCSC	5	0.4007	0.3925	0.4034	0.67	2.70
	10	0.4353	0.4264	0.4396	0.98	3.00
	50	0.4477	0.4386	0.4526	1.09	3.09
	plate	0.4482	0.4391	0.4532	1.10	3.11

Table 6
Non-dimensional symmetrical doubly-curved shell center deflection under sinusoidal loading.

BC'S	R_x/a	R_y/a	PD-HSDT (Present)	Analytical FSDT (Khdeir et al.)	Analytical HSDT (Khdeir et al.)	Relative error (%)	
						PD-HSDT	FSDT
SSSS	10	5	0.9347	0.9432	0.9328	0.21	1.11
	10	20	0.9621	0.9504	0.9597	0.25	0.97
SCSC	10	5	0.4324	0.4235	0.4365	0.93	2.98
	10	20	0.4361	0.4272	0.4405	0.99	3.02

Table 7
Non-dimensional symmetrical cylindrical shell center deflection under sinusoidal loading.

BC'S	R/a	PD-HSDT (Present)	MRZT-S	MHST	Khdeir et al. (Analytical HSDT)	Relative error (%)		
			8×8	8×8		PD-HSDT	MRZT-S	MHST
SSSS	5	0.9548	0.9392	0.9354	0.9524	0.26	1.38	1.78
	10	0.9674	0.9503	0.9473	0.9644	0.31	1.47	1.77
	50	0.9714	0.9538	0.9512	0.9683	0.32	1.49	1.77
SCSC	5	0.4448	0.4410	0.4178	0.4495	1.05	1.90	7.05
	10	0.4474	0.4435	0.4203	0.4523	1.09	1.95	7.08
	50	0.4482	0.443	0.4211	0.4532	1.11	1.96	7.09

the analytical HSDT by Khdeir et al. [55], as well as other methods, and their relative errors with Khdeir et al.'s analytical HSDT are provided. One of the other methods is called MRZT-S, which represents Bab et al. 's [56] Mixed Refined Zigzag Theory for shells. In their theory, the refined zigzag theory is implemented in the mixed finite element method. Another method is called MHST, which stands for Mixed Higher-order Shell Theory. In that theory, Bab and Kutlu [9] implemented the HSDT into the mixed finite element method. According to Table 7, for all boundary conditions and R/aratios, the current theory provides the closest results to the analytical HSDT compared to the other theories. Among all theories, the SSSS condition shows more convergent values to the analytical HSDT than the SCSC condition.

6. Conclusion

In this study, the flexural behavior of laminated composite shells is analyzed using a novel PD-HSDT framework, which combines the kinematics of HSDT with the PDDO to efficiently solve the equilibrium equations for static analysis. The principle of virtual work is employed to construct the governing equations and boundary conditions. This work represents the first application of PD-HSDT to analyze the bending response of laminated composite shells. Moreover, PD-HSDT produces better results than analytical FSDT solutions across various shell curvatures, boundary conditions, and loading scenarios. The key findings of this study can be summarized as follows.

- The capability of the current model is validated by comparing displacement, deflection, normal and transverse shear stress results, obtained with high convergence, against analytical and numerical methods available in the literature. Convergence analyses are conducted to determine suitable grid spacing and horizon size parameters.
- The static analysis results obtained via PD-HSDT successfully capture the expected behavior of laminated shells under sinusoidal and uniform loading conditions, considering doubly-curved, spherical, and cylindrical geometries, with simply supported and mixed boundary conditions. It is also observed that results for mixed boundary conditions exhibit less convergence compared to simply supported cases.
- The laminated shells analyzed consist of orthotropic materials with both symmetric and antisymmetric layering configurations. By examining stress distributions, the effect of curvature is investigated, showing that transitioning from plate to shell behavior increases asymmetry in stresses.
- The success of the approach is attributed to PDDO, which transforms local spatial derivatives in the HSDT equilibrium equations into a nonlocal form, maintaining the validity of these equations even in the presence of discontinuities. This operator eliminates the need for mesh generation, symmetric kernels, or ghost particles at boundaries, thus simplifying implementation and enhancing numerical robustness.

7. Discussion and future work

The integration of HSDT within the PDDO framework offers a powerful approach that combines the accuracy of higher-order theories with the nonlocal and mesh-free advantages of peridynamics. The current formulation enables accurate flexural analysis of laminated composite shells, effectively capturing transverse shear effects without requiring shear correction factors. This is particularly important for shear stress distributions, which are more sensitive than normal stresses and tend to exhibit abrupt variations due to changes in material properties and lamination sequences. These sharp transitions are effectively captured by the higher-order functional behavior inherent to HSDT, which aligns with the nature of such variations. PDDO complements this by enabling efficient handling of such high-order derivatives through its integral-based formulation. Its ability to model multi-layered and anisotropic composite shells demonstrates strong potential for complex structural applications.

Nonlocality is highly dependent on internal length scale parameters and discretization between material points. Hence, a proper convergence study ought to be carried out accordingly. Moreover, the present study considers only static bending analysis with linear elastic material behavior, and cylindrical, spherical and doubly-curved geometries. Future research can handle to extend the formulation for the linear/nonlinear dynamic analyses of regular/complex geometries, including conical [57], hyperbolic, and elliptic paraboloid shells. Shell structures play a crucial role in various engineering applications, such as aircraft wings, ship hulls, and pressure vessels, making accurate modeling essential for ensuring structural integrity. It is also worth noting that the nonlocal structure of the PDDO makes it suitable for incorporating progressive damage, delamination, and interlaminar failure mechanisms in composite structures. Moreover, coupling this framework with data-driven approaches, such as surrogate models or neural networks trained on PD-HSDT data, could enable efficient design optimization

and real-time predictions. This potential has been demonstrated in recent studies by Balkrishna Tandale et al. [58] and Stoffel et al. [59], which focus on intelligent stiffness estimation and structural dynamics using artificial neural networks, respectively. These works highlight the growing role of artificial intelligence in enhancing numerical methods for structural mechanics.

CRediT authorship contribution statement

Yonca Bab: Writing – review & editing, Writing – original draft, Visualization, Validation, Software, Methodology, Funding acquisition, Formal analysis, Conceptualization. **Mehmet Dorduncu:** Writing – review & editing, Visualization, Validation, Supervision, Software, Methodology, Funding acquisition, Formal analysis, Conceptualization. **Akif Kutlu:** Supervision, Methodology, Funding acquisition, Conceptualization. **Bernd Markert:** Writing – review & editing, Supervision, Conceptualization.

Declaration of competing interest

The authors declare that they have no known competing financial interests or personal relationships that could have appeared to influence the work reported in this paper.

Acknowledgements

The first author would like to acknowledge the 2214-A International Research Fellowship Programme for PhD Students, supported by the Scientific and Technological Research Council of Turkey (TÜBİTAK), under grant no. 1059B142400009. This research was also supported by the Research Foundation of Istanbul Technical University under project no. MDK-2025-46800. Open access funding provided by the RWTH Aachen University. The authors gratefully acknowledge this support.

Data availability

No data was used for the research described in the article.

References

[1] Altenbach H, Altenbach J, Kissing W. Mechanics of composite structural elements. Singapore: Springer Singapore; 2018.
[2] Jones RM. Mechanics of composite materials. CRC Press; 1999.
[3] Kaw AK. Mechanics of composite materials. 2nd ed. Boca Raton, FL: Taylor & Francis; 2006.
[4] Reddy JN. Mechanics of laminated composite plates and shells. Boca Raton: CRC Press; 2003.
[5] Reddy JN. A simple higher-order theory for laminated composite plates. J Appl Mech 1984;51:745–52. https://doi.org/10.1115/1.3167719.
[6] Wang CM, Reddy JN, Lee KH. Shear deformable beams and plates. Amsterdam: Elsevier; 2000. https://doi.org/10.1016/B978-0-08-043784-2.X5000-X.
[7] Bab Y, Kutlu A. Stress analysis of laminated HSDT beams considering bending extension coupling. Turk J Civ Eng 2023;34:1–23. https://doi.org/10.18400/tjce.1206777.
[8] Bab Y, Kutlu A. A C0 continuous mixed FE formulation for bending of laminated composite plates based on unified HSDT. Z Angew Math Mech 2023;104:1–21. https://doi.org/10.1002/zamm.202300434.
[9] Bab Y, Kutlu A. Mixed finite elements for higher-order laminated cylindrical and spherical shells. Turk J Civ Eng 2024;36:51–74. https://doi.org/10.18400/tjce.1396909.
[10] Ermis M. Warping-included mixed FE approach of beating characteristics in functionally graded graphene platelet-reinforced composite spatially curved beams under harmonic excitation force. Arch Appl Mech 2024;94:3687–713. https://doi.org/10.1007/s00419-024-02690-7.
[11] Zhao Y-F, Gao Y-S, Wang X, Markert B, Zhang S-Q. Finite element analysis of functionally graded magneto-electro-elastic porous cylindrical shells subjected to thermal loads. Mech Adv Mater Struct 2024;31:4003–18. https://doi.org/10.1080/15376494.2023.2188326.
[12] Tornabene F, Viscoti M, Dimitri R, Rabczuk T. Thermo-magneto-mechanical analysis of curved laminated structures with arbitrary variation of the material properties and novel recovery procedure. Eng Anal Bound Elem 2025;176:106232. https://doi.org/10.1016/j.enganabound.2025.106232.
[13] Gupta M, Patil ND, Kundalwal SI. Active damping of multiscale composite shells using Sinus theory incorporated with Murakami's zig-zag function. Thin-Walled Struct 2023;191:111063. https://doi.org/10.1016/j.tws.2023.111063.
[14] Ly D-K, Mahesh V, Thongchom C, Nguyen-Thoi T. Hybrid control of laminated FG-CNTRC shell structures using an advanced smoothed finite element approach based on zig-zag theory. Thin-Walled Struct 2023;184:110463. https://doi.org/10.1016/j.tws.2022.110463.
[15] Gao Y, Lei Y, He D, Yang W. A new zigzag shell model in terms of Reissner's mixed variational theorem for composite laminates with curvature. Mech Adv Mater Struct 2022;31:1–14. https://doi.org/10.1080/15376494.2022.2137888.
[16] Gao Y, Zhang H, Yang W, He D. A new bending model for composite laminated shells based on the refined zigzag theory. Arch Appl Mech 2022;92:2899–915. https://doi.org/10.1007/s00419-022-02210-5.
[17] Zhang H, Gao Y, He D, Yang W. Free vibration and buckling analysis of composite laminated shells using the refined zigzag theory. J Theor Appl Mech 2022;60:435–48. https://doi.org/10.15632/jtam-pl/150847.
[18] Tessler A, Di Sciuva M, Gherlone M. A refined zigzag beam theory for composite and sandwich beams. J Compos Mater 2009;43:1051–81. https://doi.org/10.1177/0021998308097730.
[19] Tessler A, Di Sciuva M, Gherlone M. A consistent refinement of first-order shear deformation theory for laminated composite and sandwich plates using improved zigzag kinematics. J Mech Mater Struct 2010;5:341–67. https://doi.org/10.2140/jomms.2010.5.341.
[20] Tessler A, Di Sciuva M, Gherlone M. A homogeneous limit methodology and refinements of computationally efficient zigzag theory for homogeneous, laminated composite, and sandwich plates. Numer Methods Part Differ Equ 2011;27:208–29. https://doi.org/10.1002/num.20646.
[21] Tessler A. Refined zigzag theory for homogeneous, laminated composite, and sandwich beams derived from Reissner's mixed variational principle. Meccanica 2015;50:2621–48. https://doi.org/10.1007/s11012-015-0222-0.
[22] Ermis M, Dorduncu M, Aydogan G. Physics-based machine learning for modeling of laminated composite plates based on refined zigzag theory. Arch Appl Mech 2025;95:107. https://doi.org/10.1007/s00419-025-02816-5.
[23] Carrera E. Theories and finite elements for multilayered plates and shells:A unified compact formulation with numerical assessment and benchmarking. ARCO 2003;10:215–96. https://doi.org/10.1007/BF02736224.
[24] Carrera E, Giunta G. Refined beam theories based on a unified formulation. Int J Appl Mechanics 2010;02:117–43. https://doi.org/10.1142/S1758825110000500.
[25] Mir O, Farrokh Mojtaba, Carrera E. Mechanical buckling load of the stiffened cylindrical structures using higher-order CUF refined beam approach. Mech Adv Mater Struct 2025;0:1–11. https://doi.org/10.1080/15376494.2024.2443815.
[26] Mohammed MNA, Augello R, Demirbas MD, Carrera E. Delamination analysis of functionally graded materials using Carrera Unified Formulation and Cohesive Zone model. Compos Struct 2025;365:119147. https://doi.org/10.1016/j.compstruct.2025.119147.
[27] Ferreira AJM. A formulation of the multiquadric radial basis function method for the analysis of laminated composite plates. Compos Struct 2003;59:385–92. https://doi.org/10.1016/S0263-8223(02)00239-8.
[28] Dorduncu M, Ren H, Zhuang X, Silling S, Madenci E, Rabczuk T. A review of peridynamic theory and nonlocal operators along with their computer implementations. Comput Struct 2024;299:107395. https://doi.org/10.1016/j.compstruc.2024.107395.
[29] Hu YL, Carvalho NVD, Madenci E. Peridynamic modeling of delamination growth in composite laminates. Compos Struct 2015;132:610–20. https://doi.org/10.1016/j.compstruct.2015.05.079.
[30] Diyaroglu C, Oterkus E, Madenci E, Rabczuk T, Siddiq A. Peridynamic modeling of composite laminates under explosive loading. Compos Struct 2016;144:14–23. https://doi.org/10.1016/j.compstruct.2016.02.018.
[31] Hu YL, Yu Y, Madenci E. Peridynamic modeling of composite laminates with material coupling and transverse shear deformation. Compos Struct 2020;253:112760. https://doi.org/10.1016/j.compstruct.2020.112760.
[32] Zhang G, Dai Z. A novel fracture model for composite laminates based on bond-based peridynamics. Eng Anal Bound Elem 2025;176:106229. https://doi.org/10.1016/j.enganabound.2025.106229.
[33] Rabczuk T, Ren H, Zhuang X. A nonlocal operator method for partial differential equations with application to electromagnetic waveguide problem. Comput Mater Contin 2019;59:31–55. https://doi.org/10.32604/cmc.2019.04567.
[34] Ray MC. Mesh-free models for static analysis of smart laminated composite beams. Int J Numer Methods Eng 2017;109:1804–20. https://doi.org/10.1002/nme.5357.
[35] Madenci E, Dorduncu M, Gu X. Peridynamic least squares minimization. Comput Methods Appl Mech Eng 2019;348:846–74. https://doi.org/10.1016/j.cma.2019.01.032.
[36] Žur KK, Faghidian SA. Nanomechanics of structures and materials: modeling and analysis. Elsevier; 2024.
[37] Madenci E, Dorduncu M, Barut A, Futch M. Numerical solution of linear and nonlinear partial differential equations using the peridynamic differential operator. Numer Methods Part Differ Equ 2017;33:1726–53. https://doi.org/10.1002/num.22167.
[38] Madenci E, Barut A, Futch M. Peridynamic differential operator and its applications. Comput Methods Appl Mech Eng 2016;304:408–51. https://doi.org/10.1016/j.cma.2016.02.028.
[39] Madenci E, Barut A, Dorduncu M. Peridynamic differential operator for numerical analysis, 10. Berlin: Springer International Publishing; 2019. https://doi.org/10.1007/978-3-030-02647-9.
[40] Shojaei A, Galvanetto U, Rabczuk T, Jenabi A, Zaccariotto M. A generalized finite difference method based on the peridynamic differential operator for the solution

of problems in bounded and unbounded domains. Comput Methods Appl Mech Eng 2019;343:100–26. https://doi.org/10.1016/j.cma.2018.08.033.
[41] Barretta R, Faghidian SA, Marotti de Sciarra F. A consistent variational formulation of Bishop nonlocal rods. Contin Mech Thermodyn 2020;32:1311–23. https://doi.org/10.1007/s00161-019-00843-6.
[42] Faghidian SA, Elishakoff I. Wave propagation in Timoshenko–Ehrenfest Nanobeam: a mixture unified gradient theory. J Vib Acoust 2022;144:061005. https://doi.org/10.1115/1.4055805.
[43] Dorduncu M. Stress analysis of laminated composite beams using refined zigzag theory and peridynamic differential operator. Compos Struct 2019;218:193–203. https://doi.org/10.1016/j.compstruct.2019.03.035.
[44] Ermis M, Dorduncu M, Kutlu A. Peridynamic differential operator for stress analysis of imperfect functionally graded porous sandwich beams based on refined zigzag theory. Appl Math Model 2024;133:414–35. https://doi.org/10.1016/j.apm.2024.05.032.
[45] Challamel N, Wang CM, Reddy JN, Faghidian SA. Equivalence between micromorphic, nonlocal gradient, and two-phase nonlocal beam theories. Acta Mech 2024;236:871–902. https://doi.org/10.1007/s00707-024-04180-x.
[46] Silling SA. Reformulation of elasticity theory for discontinuities and long-range forces. J Mech Phys Solids 2000;48:175–209. https://doi.org/10.1016/S0022-5096(99)00029-0.
[47] Silling SA, Epton M, Weckner O, Xu J, Askari E. Peridynamic states and constitutive modeling. J Elast 2007;88:151–84. https://doi.org/10.1007/s10659-007-9125-1.
[48] Dorduncu M, Kutlu A, Madenci E, Rabczuk T. Nonlocal modeling of bi-material and modulus graded plates using peridynamic differential operator. Eng Comput 2022:1–17. https://doi.org/10.1007/s00366-022-01699-2.
[49] Faghidian SA. Unified formulation of the stress field of saint-Venant's flexure problem for symmetric cross-sections. Int J Mech Sci 2016;111:65–72. https://doi.org/10.1016/j.ijmecsci.2016.04.003.
[50] Reddy JN, Liu CF. A higher-order shear deformation theory of laminated elastic shells. Int J Eng Sci 1985;23:319–30. https://doi.org/10.1016/0020-7225(85)90051-5.
[51] Sayyad AS, Ghugal YM. Static and free vibration analysis of laminated composite and sandwich spherical shells using a generalized higher-order shell theory. Compos Struct 2019;219:129–46. https://doi.org/10.1016/j.compstruct.2019.03.054.
[52] Dorduncu M, Kutlu A, Madenci E. Triangular C0 continuous finite elements based on refined zigzag theory {2,2} for free and forced vibration analyses of laminated plates. Compos Struct 2022;281:115058. https://doi.org/10.1016/j.compstruct.2021.115058.
[53] Sadd MH. Elasticity: theory, applications, and numerics. 2nd ed. Amsterdam; Boston: Elsevier/AP; 2009.
[54] Reddy N, Liu F. A higher-order theory for geometrically nonlinear analysis of composite laminates. NASA Contract. Rep. 1987;4056.
[55] Khdeir AA, Librescu L, Frederick D. A shear deformable theory of laminated composite shallow shell-type panels and their response analysis II: static response. Acta Mech 1989;77:1–12. https://doi.org/10.1007/BF01379740.
[56] Bab Y, Kutlu A, Dorduncu M. Mixed finite element formulation for laminated composite cylindrical shells based on refined zigzag theory. In: The 9th European Congress on computational methods in applied sciences and engineering ECCOMAS Congress; 2024.
[57] Tariq MH, Bibi A, Ge J, Wang L, Zhou Y-T. Coupling of poro-electro-elastic effects in a conical shell under various loadings at its apex. Eng Anal Bound Elem 2025;178:106300. https://doi.org/10.1016/j.enganabound.2025.106300.
[58] Balkrishna Tandale S, Markert B, Stoffel M. Intelligent stiffness computation for plate and beam structures by neural network enhanced finite element analysis. Int J Numer Methods Eng 2022;123:4001–31. https://doi.org/10.1002/nme.6996.
[59] Stoffel M, Gulakala R, Bamer F, Markert B. Artificial neural networks in structural dynamics: a new modular radial basis function approach vs. convolutional and feedforward topologies. Comput Methods Appl Mech Eng 2020;364:112989. https://doi.org/10.1016/j.cma.2020.112989.